Macromolecules

pubs.acs.org/Macromolecules Article

Effects of Coarse-Graining on Molecular Simulation of Craze Formation in Polymer Glass

Jiuling Wang, Pieter J. in 't Veld, Mark O. Robbins, and Ting Ge*

Cite This: *Macromolecules* 2022, 55, 1267−1278 Read Online

ACCESS | Metrics & More | Article Recommendations | Supporting Information

ABSTRACT: Crazing precedes the crack propagation in polymer glass and greatly increases the fracture toughness. We perform molecular dynamics simulations to study craze formation in glassy polystyrene (PS). The use of a structure-based coarse-grained (CG) model allows us to create and equilibrate a large-scale sample (≈ 71 nm × 71 nm × 71 nm) of well-entangled PS chains with molecular weight 10 times the entanglement threshold. The back-mapping of the CG sample to the united-atom (UA) representation generates a PS sample with fine atomistic details. The structural features of the craze fibrils in the CG and UA simulations are almost the same, and both correlate with the underlying entanglement network as in the traditional theoretical description, reflecting the preservation of structural correlations during the coarse-graining. The stress level in the CG simulation is reduced compared with the UA simulation, as the coarse-graining with fine atomistic details removed leads to a smoother potential energy landscape for craze formation. In both CG and UA simulations, the same large fraction (70%−80%) of the stress during craze formation is dissipative stress, suggesting the coarse-graining preserves the relative contributions of the energetic and dissipative components to the overall stress. The constant drawing stress is related to the surface tension and the average spacing between craze fibrils in the simulations, as in the traditional models of crazing. We also demonstrate a scale-bridging simulation protocol where the CG simulation is used to accelerate the craze formation, and the subsequent back-mapping to the UA simulation is used to recover the stress level.

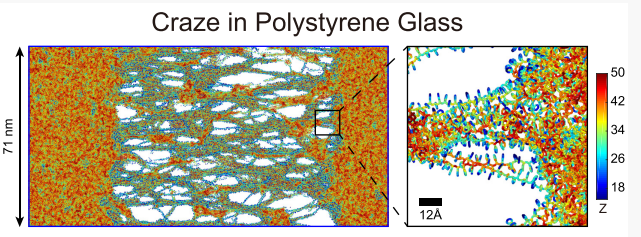

1. INTRODUCTION

Molecular simulations of high-molecular-weight polymers are challenging because of the broad range of length and time scales relevant to the behavior of polymers. To accelerate the simulations of polymers, coarse-grained (CG) polymer models have been developed,[1−3] where a group of atoms ranging from a fraction of a chemical monomer to multiple chemical monomers are replaced by a CG bead. The acceleration arises from the decrease in the total number of atoms, the use of a larger time step for the evolution of molecular dynamics, and the smoothing of the interatomic potential energy landscape. CG polymer models have been developed by using different schemes[4−21] and employed to simulate the dynamics and rheological properties[17−19,22−29] of polymers above the glass transition temperature T_g as well as the mechanical properties[30−37] of glassy polymers below T_g. The CG simulations have fostered the understanding of microscopic mechanisms underlying the macroscopic properties of polymers, which are otherwise difficult to explore with fully atomistic simulations.

In this paper, we examine the performance of a chemically specific CG model in the simulations of craze formation, which is a unique mechanical failure mechanism of high-molecular-weight glassy polymers.[38−61] Prior to the ultimate crack propagation, crazing converts dense polymer glass into fibrils with voids between them and greatly enhances the fracture toughness of polymer glass.[39,40,47,62,63] The entanglement network underlying a high-molecular-weight polymer glass plays an essential role in crazing by controlling the extension ratio of the craze fibrils with respect to the dense glass and determining the spacing between the fibrils.[38,40−42,48,58] The microscopic picture of the crazing process has been studied by molecular simulations using the generic CG bead−spring model in polymer physics.[47,48,58,64−67] While many common features of the crazing in chemically different glassy polymers have been captured by the simulations, the lack of atomistic details prevents a direct comparison of simulations and experiments.

We perform large-scale molecular simulations of craze formation in polystyrene (PS) glass using a structure-based CG model and a united-atom (UA) model. The usage of the CG model allowed us to build and equilibrate a large sample of well-entangled PS molecules. The subsequent back-mapping to the UA representation followed by a short equilibration of local configurations created a well-entangled UA sample. The

Received: September 17, 2021
Revised: January 9, 2022
Published: February 1, 2022

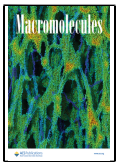

https://doi.org/10.1021/acs.macromol.1c01969
Macromolecules 2022, 55, 1267−1278

comparison of the CG and UA simulations demonstrates that coarse-graining preserves the characteristic structural features of polymer craze, which compare well with the experimental data, but lowers the stress level, including the drawing stress during the craze formation. Detailed analysis of the simulation results provides a numerical evaluation of existing microscopic models[38,40−42] of polymer crazing. We also demonstrate the feasibility of a scale-bridging simulation where the CG simulation is used to produce the fibril structure and the subsequent UA simulation is used to recover the stress level. Section 2 describes the CG and UA models of PS and the methods for sample preparation and crazing simulation. Section 3 presents the simulation results and discussion. Conclusions are given in section 4.

2. MODEL AND METHODOLOGY

2.1. Models of Polystyrene. In the united-atom (UA) model of PS, as shown in Figure 1a, only carbon atoms are retained, while the hydrogen atoms in the fully atomistic representation are merged with the connected carbon atoms. This representation improves the computational efficiency with respect to the fully atomistic simulation by reducing the number density of atoms and the average number of neighbors. The force field parameters developed by Mondello et al.[68] are used in our UA simulations.

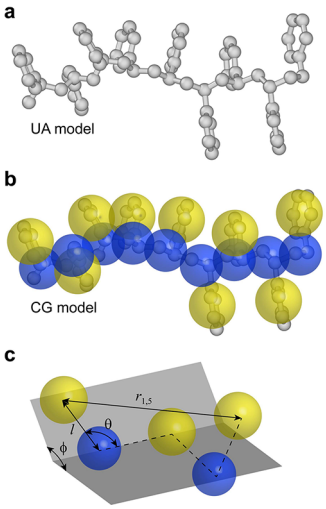

Figure 1. Schematic illustration of the UA and CG models of PS. (a) In the UA model, hydrogen atoms are merged with connected carbons to yield united atoms (gray spheres). (b) In the CG model, two types of CG beads (blue and yellow spheres) are used to represent the backbone and side groups, respectively. (c) The bond length l, bond angle θ, dihedral angle ϕ, and the 1,5-pairwise distance $r_{1,5}$ are indicated for the CG model. Dashed black lines indicate the bonds between the CG beads.

We employ the CG model developed by Agrawal et al.[69] In the CG model, two types of CG beads are used to represent a polymer chain, as illustrated in Figure 1b. The two types of CG beads correspond to the backbone and side groups, respectively. This mapping from a chemical monomer to a CG representation captures the steric effects of side phenyl groups.[22,70] Subtypes of the CG beads for side groups are introduced to capture tacticity. Although isotactic and syndiotactic PS can be simulated by using this CG model, we focus on atactic PS. The CG beads in a polymer chain alternate from one type to the other, resulting in an effectively linear polymer. This linear topology facilitates the implementation of various algorithms developed for the equilibration of high-molecular-weight linear polymers.

For the CG representation in Figure 1b, the structural correlations up to at least five consecutive CG beads are required for accurate modeling of the stereochemistry of atactic PS, as demonstrated by Fritz et al.[71] As illustrated in Figure 1c, among five consecutive beads, there are bonding interaction $U(l)$, bending potential $U(\theta)$, torsional potential $U(\phi)$, and 1,5-pairwise potential $U(r_{1,5})$, where l is the bond length between two neighboring beads, θ is the angle between two successive bonds, ϕ is the dihedral angle, and $r_{1,5}$ is the distance between a bead and its fourth nearest neighbor along the chain. In particular, the 1,5-pairwise interaction has been shown to be necessary for the rigidity of PS.[69,71] In the development of the CG force fields, the iterative Boltzmann inversion (IBI) method was used to reproduce the probability distributions of l, θ, ϕ, and $r_{1,5}$ in the all-atom (AA) simulations of PS at temperature T = 500 K. In addition to the bonded interactions, a nonbonded pairwise interaction $U(r)$ exists between the CG beads that are separated by more than four beads in the same chain and the CG beads from different chains. The IBI method was used to construct $U(r)$ such that the radial distribution function for the CG beads in the AA simulations at T = 500 K was reproduced.

2.2. Sample Preparation. The large CG PS sample consists of M = 1200 chains with N = 3520 CG beads per chain, corresponding to a total of 4224000 CG beads. The number of monomers per chain $N/2$ = 1760, and the molecular weight M_w = 183 kg/mol. Because the entanglement molecular weight M_e of PS is 17 kg/mol, $M_w \approx 10M_e$, indicating the PS chains are well entangled. Such a large-scale and well-entangled simulation sample with atomistic details represents the state of the art. As a comparison, in a recently published paper on the modeling of long entangled polyisoprene (PI) melts,[29] the largest simulation sample contains M = 200 PI chains with 500 monomers per chain.

The CG PS chains were generated by using the enhanced Monte Carlo (EMC) builder developed by In 't Veld.[72,73] Periodic boundary conditions were applied to the x-, y-, and z-directions. The equilibration of polymer chains was performed at temperature T = 503 K and density ρ_{melt} = 0.94 g/cm^3 with the built-in MC algorithms. After the sample generation and equilibration using the EMC builder, the melt density was adjusted by a short NPT simulation, where the Nosé−Hoover thermostat with a damping parameter of 0.1 ps was used to maintain the temperature at T = 503 K, and the Nosé−Hoover barostat with a damping parameter of 5 ps was used to maintain the pressure at p = 1 atm. The cutoff distance for nonbonded pairwise potentials $U(r)$ is 10 Å. The velocity-Verlet algorithm was utilized to perform time integration with a time step 0.002 ps. After a NPT simulation of 200 ps, the melt density was stabilized at ρ_{melt} = 0.95 g/cm^3 with the dimensions of the simulation box $L_x = L_y = L_z$ = 727 Å.

The UA sample was obtained by inserting the atomistic details (see Figure 1a) into the CG sample. Different back-mapping schemes have been used in the literature.[74−82] Our back-mapping from CG to UA representations tends to introduce large distortions of local structures and overlapping between atoms. As a result, an energy minimization was performed to adjust the local configurations.[30] The UA sample was equilibrated at T = 503 K and P = 1 atm by using the

https://doi.org/10.1021/acs.macromol.1c01969
Macromolecules 2022, 55, 1267−1278

Nosé−Hoover thermostat and barostat. The damping parameter was 0.1 ps for the thermostat and 5 ps for the barostat. The cutoff distance for all the pairwise Lennard-Jones interactions between nonbonded atoms was 12 Å, and the time step was 0.002 ps in the simulations. The short equilibration lasted for 2×10^4 ps. The simulation time allowed the UA system to sample different configurations at length scales below the monomer length, while the chain conformations at length scales above the monomer length were preserved. After the equilibration, $\rho_{melt} = 0.97$ g/cm^3 and $L_x = L_y = L_z = 723$ Å.

Equilibrating a UA sample built from the scratch without the use of the pre-equilibrated CG sample would require much more computational effort. Previously, we reported the mean-squared displacement (MSD) of monomers as a function of time in the UA simulation of a PS melt.[30] From the MSD result at $T = 503$ K, the monomeric time for the MSD to be comparable to the square of the monomer size is $\tau_{mon} \approx 10^4$ ps. By use of the scaling relation in the Rouse model for unentangled polymer dynamics, the entanglement time, which is the Rouse relaxation time of an entanglement strand of 163 monomers, is $\tau_e \approx 163^2 \tau_{mon} \approx 2.7 \times 10^8$ ps. By use of the scaling relation in the reptation model for entangled polymer dynamics, the terminal relaxation time, which is the reptation time of the 1760 monomers, is $\tau_{rep} \approx (1760/163)^3 \tau_e \approx 3.4 \times 10^{11}$ps ≈ 0.3 s. Because a simulation of at least a few terminal relaxation time is needed to relax the initial conformations of UA chains, we estimate that the equilibration time would be comparable to 1 s. The estimated time is well beyond the current capability of computing power that usually can handle a simulation up to only the order of 1 μs. An alternative method of equilibrating a UA sample built from the scratch would be the use of MC algorithms. The MC algorithms in the EMC builder can handle linear bond connectivity as in the CG PS model we use (see Figure 1) but would need to be revised to handle the nonlinear bond connectivity such as the benzene rings in the UA PS model. With the possibility of equilibrating a UA PS sample by using a pure MD simulation or the EMC builder excluded, the method based on back-mapping the pre-equilibrated CG sample is the only viable option.

The equilibrated CG and UA samples were quenched at a cooling rate of 0.1 K/ps from $T = 503$ K to $T = 300$ K. The rate 0.1 K/ps enables a fast quenching with respect to the mobility of monomers, as demonstrated previously[30] by comparing the MSD of monomers during the quenching and the size of a monomer. The glass transition temperature $T_g \approx 320$ K for the CG and UA samples, which was extracted from the plot of the specific volume per monomer as a function of temperature by using the standard protocol.[30]

We characterize the conformations of polymer chains using $\langle R^2(n)\rangle/(nl_0^2)$, where n is the number of carbon atoms along the backbone of a PS chain segment, $\langle R^2(n)\rangle$ is the mean-square end-to-end size of chain segments, and $l_0 = 1.574$ Å is the bond length between backbone carbon atoms. The results for the CG and UA samples at $T = 300$ K are shown in Figure 2. PS chains in the two samples exhibit almost the same conformations, which is expected as the UA sample was build from the CG sample. The monotonic increase with n and the subsequent leveling off at large n indicate the samples were well equilibrated, as discussed by Auhl et al.[83] The characteristic ratio $C_\infty = \lim_{n\to\infty}\langle R^2(n)\rangle/(nl_0^2) = 9.5$ is close to the value $C_\infty = 10$ for PS in experiments.[84]

2.3. Crazing Simulation. The PS samples at 300 K were used in the crazing simulations. The deformation protocol of crazing was the same as in the previous simulations[47,48,58,64−66,85] using the bead−spring polymer model. The box dimensions L_x and L_y along the x- and y-directions were kept constant, while the box dimension L_z along the z-direction was increased. This led to triaxial tensile stress, which is generally required to induce cavitation and subsequent crazing.[38,86] The deformation velocity was held constant at $v = dL_z/dz = 10^{-5}$ Å/fs = 1 m/s in the CG simulation and 2 m/s in the UA simulation. Reference 30 shows that the monomeric length scale is $\sigma_{mon} = 5.5$ Å, and the time τ_{mon} for the monomers to diffuse by a distance of σ_{mon} is larger than 10^5 ps at 300 K. With $v = O(1)$ m/s in both the CG and UA simulations, the time for a monomer to move by σ_{mon} upon deformation is $\sigma_{mon}/v = O(100)$ ps. This time is much shorter than τ_{mon}, indicating that the monomers do not have time to thermally diffuse during the imposed deformation. The tensile stress σ_z was recorded as a function of the stretch factor $\lambda = L_z/L_z^0$, where L_z^0 is the initial box size along the z-direction. $L_z^0 = 710$ and 711 Å for the CG and UA samples, respectively. Note that L_z^0 is slightly different from L_z of the melt. A Langevin thermostat with $T = 300$ K and damping parameter 100 fs was applied to the x- and y-directions perpendicular to the stretching direction. The time step was 0.002 ps in both CG and UA simulations. All the simulations were performed by using the LAMMPS package.[87] During the deformation simulation, craze fibrils nucleated and grew between two dense glassy regions. Snapshots of the coexistence of crazed and uncrazed regions in the CG and UA simulations are shown in Figures 3a and 3b, respectively. Movies visualizing the craze formation in the two sets of simulations are provided as Supporting Information.

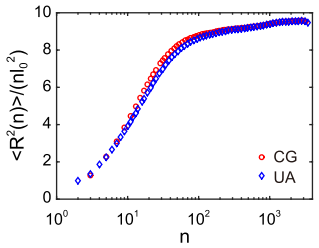

Figure 2. $\langle R^2(n)\rangle/(nl_0^2)$ as a function of n for the CG and UA samples at $T = 300$ K, where n is the number of carbon atoms along the backbone of a PS chain segment, $\langle R^2(n)\rangle$ is the mean-square end-to-end size of chain segments, and $l_0 = 1.574$ Å is the bond length between backbone carbon atoms. The characteristic ratio $C_\infty = \lim_{n\to\infty}\langle R^2(n)\rangle/(nl_0^2) = 9.5$.

2.4. Characterization of Craze Fibrils. We characterize the structure of craze fibrils using two methods. In method I, a polymer craze is divided into consecutive cross sections of thickness 7 Å ($\approx 1.3\sigma_{mon}$) along the z-direction. In each cross section, the monomers (C_8H_8) are represented by their centers of mass. The monomer centers are projected to the xy-plane and grouped into different clusters based on the distances between the monomers in the xy-plane. Two monomers belong to the same cluster if they are separated by a distance less than 10 Å. Each cluster constructed in this way represents a cross section of a craze fibril. To determine the cross-sectional area A of a cluster, the xy-plane is divided into a two-dimensional array of squares with each square covering an area of $a_0^2 = 1$ Å $\times$ 1 Å. The cross-sectional area A is the sum of the areas of all the squares that are within 5 Å from at least one monomer in the cluster. The diameter of a fibril cross section is

https://doi.org/10.1021/acs.macromol.1c01969
Macromolecules 2022, 55, 1267−1278

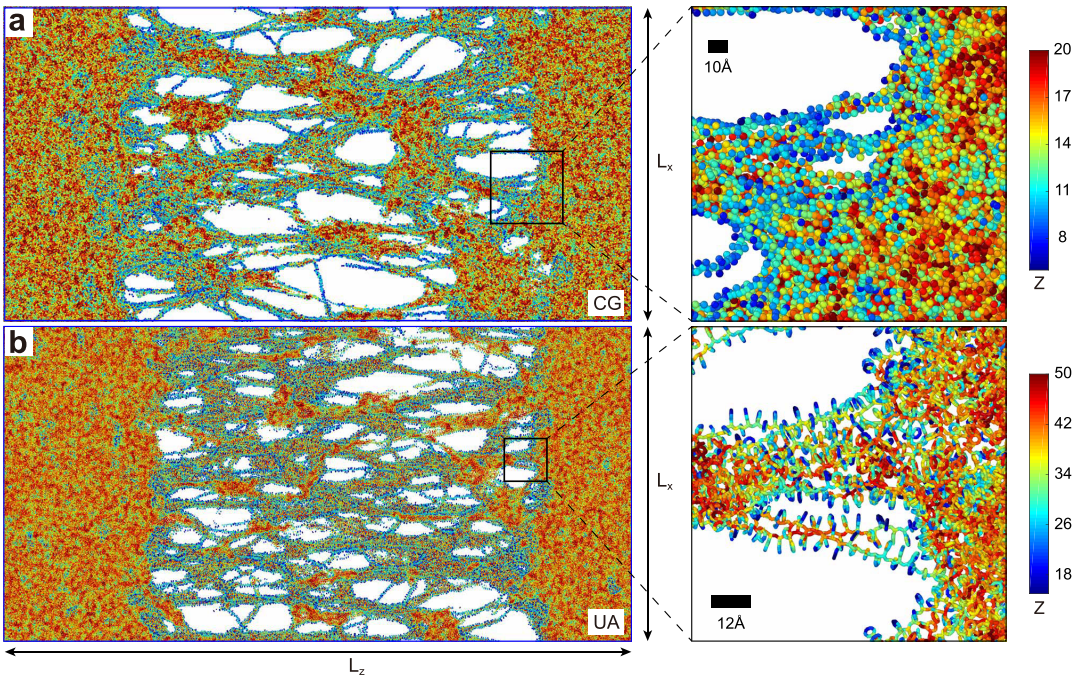

Figure 3. Snapshots of the coexistence of crazed and uncrazed regions in the (a) CG and (b) UA simulations of PS crazing at T = 300 K. L_x = 710 and 711 Å for the CG and UA samples, respectively. $L_z = \lambda L_z^0$ with $L_z^0 = L_x$ and the stretch factor λ = 2. The polymer beads are colored based on the coordination number Z, i.e., the number of neighboring beads. For clarity, only beads in a slab of thickness 100 Å in the y-direction are shown. Right panels are enlarged views of selected regions at the interface between crazed and uncrazed regions. The scale bars indicate the cutoff distances used in the simulations.

estimated as $D = \sqrt{4A/\pi}$.[48] The average spacing between fibrils is estimated as $\langle D_0 \rangle = \sqrt{4L_xL_y/\pi\langle m \rangle}$, where $\langle m \rangle$ is the average number of fibrils (clusters) per cross section. This method was motivated by the approximation of craze fibrils as a forest of cylinders in the theoretical models of crazing[38,40−42] and was adopted by Rottler and Robbins in their analysis of the craze fibrils in the bead−spring polymer simulations.[48] Here, we extend the analysis by calculating the perimeter P of each cluster and then estimating the surface area of all fibrils. In the calculation of P, a square in a cluster is considered as one on the perimeter if it is surrounded by fewer than four squares in the same cluster. Following the protocol developed by Pastewka and Robbins,[88] the perimeter of a cluster is determined to be $P = \beta a_0 N_P$, where N_P is the number of squares on the perimeter, a_0 = 1 Å is the side length of a square, and β = 1.1222 is the correction factor. The total surface area of all fibrils is estimated as $\int_0^{L_z} P_t(z)\, dz$, where $P_t(z)$ is the sum of the perimeters of all clusters in the cross section located at z.

In method II, we compute the structure factor $S(\mathbf{k})$ of a craze, as in the scattering experiments using X-rays or electrons.[38,40] $S(\mathbf{k}) = \frac{1}{N}\langle \sum_{\alpha,\beta} e^{-i\mathbf{k}\cdot(\mathbf{r}_\alpha - \mathbf{r}_\beta)} \rangle$, where the subscripts α and β indicate two different monomers, $\mathbf{r}_\alpha$ and $\mathbf{r}_\beta$ are the centers of mass of the two monomers, $\mathbf{k}$ is the wave vector, and N is the total number of monomers in the simulation box. $\mathbf{k}$ is decomposed into $k_\parallel$ and $k_\perp$, which are the components parallel and perpendicular to the z-direction for deformation. Because we are interested in the structure within the xy-plane, we set $k_\parallel$ = 0 and compute $S(k_\perp)$.

3. RESULTS AND DISCUSSION

3.1. Stress−Strain Behavior. Stress−stretch curves in Figure 4 for PS crazing in the CG and UA simulations both exhibit features similar to that in the previous bead−spring polymer simulations.[48] With increasing stretch λ, the tensile stress σ_z first rises to a yield peak σ_Y and then drops as craze nucleates by cavitation in the glass. This stage of the stress−stretch curve is enlarged in Figure 4b for $1 < \lambda < 1.16$. Later, σ_z remains at a constant value S as the glassy polymers are progressively converted to craze fibrils. Finally, σ_z rises again as the fully developed craze is stretched. The simulations stopped before any bonds are stretched to the breaking point. The ultimate failure of polymer craze via bond scission cannot be simulated, as no bond breaking is allowed in the CG and UA models.

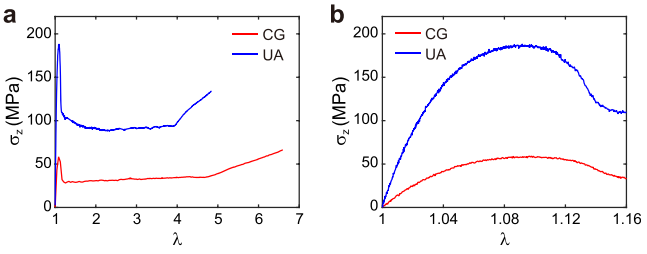

Figure 4. Tensile stress σ_z as a function of stretch factor λ for PS crazing in the CG and UA simulations. (b) Enlarged view of the stress−stretch curve for $1 < \lambda < 1.16$.

At all stages of the stress−stretch curve, the stress level in the CG simulation is lower than that in the UA simulation. This is consistent with the previous simulations that demonstrated the stress level during the plastic deformation

https://doi.org/10.1021/acs.macromol.1c01969
Macromolecules 2022, 55, 1267−1278

Table 1. Comparison of PS Crazes in Simulations and Experiments[a]

	plateau stress S (MPa)	extension ratio Λ	fibril diameter from direct image (Å)	average fibril diameter from scattering $\langle D\rangle$ (Å)	fibril spacing (Å)	surface energy Γ (mN/m)
CG model	34	4.9	35 ($\langle D\rangle$ in method I)	16.3 (method II)	102 ($\langle D_0\rangle$ in method I)	21.5
UA model	91	4.2	33 ($\langle D\rangle$ in method I)	13.3 (method II)	90 ($\langle D_0\rangle$ in method I)	54.7
experiments	35	4	40−100 (TEM)	60 (X-ray scattering)	200−300 (TEM)	40

[a]The simulations and experiments were performed at different strain rates.

of a PS glass under uniaxial compression or simple shear decreases with increasing degree of coarse-graining.[30] For the yield stress, Figure 4b shows σ_Y = 59 and 180 MPa for the CG and UA samples, respectively. A direct comparison of σ_Y in the simulations and experiments is not given here, as σ_Y depends on the strain rate and thermal history of a sample,[86,89−92] and it is difficult to match the simulations and experiments in terms of both.

For the constant drawing stress S, Figure 4a shows S_{CG} = 34 MPa in the CG simulation is below S_{UA} = 91 MPa in the UA simulation. S is not affected by the thermal history before deformation and is independent of temperature if it is well below T_g. Previous experiments[38,40] in the temperature range 300−330 K showed that the drawing stress is $S_{exp} \approx 35$ MPa for a PS glass of molecular weight 1800 kg/mol deformed at a strain rate $O(10^{-6})$ s^{-1}. A comparison of the simulation and experiment results of the drawing stress and other physical properties of PS craze is in Table 1. Although S_{CG} = 34 MPa agrees well with the experimental value, we view it as a coincidence due to two effects that change S in opposite directions. On one hand, S_{CG} is smaller than S_{UA} at similar deformation velocity $v = O(1)$ ms^{-1} because the degrees of freedom that can store and dissipate energy upon deformation are both reduced by the coarse-graining, and thus the associated contributions to the stress are reduced. On the other hand, the deformation velocity $v = O(1)$ ms^{-1} for a simulation box of size $O(10^3)$ Å yields a deformation rate $O(10^7)$ s^{-1} that is 13 orders of magnitude faster than $O(10^{-6})$ s^{-1} in the experiment, and as a result the stress level is raised by the much faster deformation. The effects of coarse-graining and deformation rate on the stress level counterbalance each other, coincidentally leading to $S_{CG} \approx S_{exp}$.

We further study the dependence of S_{CG} on v by adding a set of short CG simulations at different values of v. The CG sample with coexisting craze fibrils and dense glass, which was obtained with v = 1 m/s, was further deformed with a different value of v. After a short run, a new drawing stress S_{CG} was reached. Figure 5 shows S_{CG} as a function of v. In a range of v spanning over 1 order of magnitude, S_{CG} depends logarithmically on v, as indicated by the dashed line in Figure 5. This weak logarithmic dependence of stress on strain rate has been observed both in the simulations using the bead−spring model[48] and in more recent simulations of PS glasses under simple shear[30] and may be interpreted by using an Eyring model of stress-biased thermal activation. Extrapolating the best fit S_{CG}/MPa = 33.95 + 2.86 ln [v/(m s^{-1})] to a deformation velocity 13 orders of magnitude slower than $O(1)$ ms^{-1} would give a negative stress value. This suggests that the observed logarithmic rate dependence has a lower bound, which presumably is related to the competition with

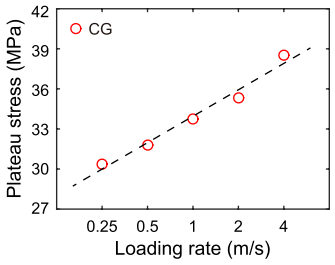

Figure 5. Loading rate dependence of the plateau stress S_{CG} in the CG simulations. The dashed line is the best fit to a logarithmic rate dependence, S_{CG}/MPa = 33.95 + 2.86 ln [v/(m s^{-1})].

the diffusion time scale τ_{mon} as the deformation rate approaches $O(\tau_{mon}^{-1})$. Deformation rates in previous molecular dynamics simulations[16,93] were also higher than typical experimental values by orders of magnitude, but an agreement between the stress levels in the simulations and experiments has also been reported.

3.2. Extension Ratio. A polymer craze is characterized by a constant extension ratio Λ with respect to the uncrazed dense glass. As illustrated in Figure 3 and the movies in the Supporting Information, uncrazed dense glass and craze fibrils coexist during crazing. This is further demonstrated by the normalized density profiles in Figure 6, where the normalized

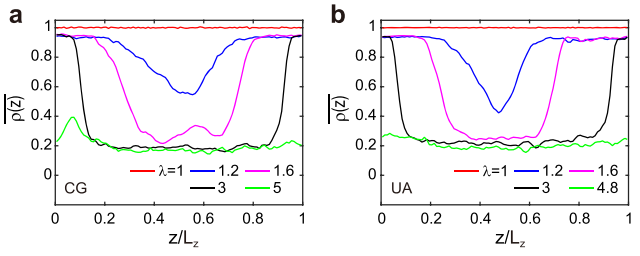

Figure 6. Normalized density profiles $\overline{\rho(z)}$ along the stretch direction (z-direction) during craze growth in the (a) CG and (b) UA simulations. $\overline{\rho(z)} = \rho(z)/\rho_{glass}$, where $\rho(z)$ is the mass density at z and ρ_{glass} is the mass density of PS before the deformation. ρ_{glass} = 1.02 g/cm^3 for both the CG and UA samples.

density $\rho_{craze}/\rho_{glass}$ of the crazed region is smaller than $\rho_{uncraze}/\rho_{glass}$ of the uncrazed region. The extension ratio of the craze fibrils is computed as $\Lambda = \rho_{uncraze}/\rho_{craze}$. We obtain Λ_{CG} = 4.9 for the CG sample and Λ_{UA} = 4.2 for the UA sample. Λ of the craze coincides with the end of the plateau region in the stress−stretch curves (Figure 4), where all the dense glass has just been drawn to craze fibrils. From the end of the plateau, we estimate Λ_{CG} = 4.7 for the CG sample and Λ_{UA} = 4.0 for the UA sample, which are close to the respective values extracted from the density plots. The range of extension ratio

https://doi.org/10.1021/acs.macromol.1c01969
Macromolecules 2022, 55, 1267−1278

Λ = 4.0−4.9 in the simulations is comparable to the experimental value 4 of the PS craze[38,40] (see Table 1).

Experiments[38,40] have shown that Λ approximately equals the maximum extension ratio λ_{max} of a network strand in the entanglement network. The length of a fully stretched network strand with n_e backbone carbon atoms is $l_e = n_e l_0 \sin(\theta/2)$ with the angle between two neighboring carbon−carbon bonds $\theta \approx 109.5°$. l_e does not equal $n_e l_0$, as the fully stretched network strand is not a straight line but is in a zigzag conformation, as illustrated in Figure 1a. The root-mean-square end-to-end distance of the strand is $d_e = \sqrt{C_\infty n_e l_0^2}$. As a result, $\lambda_{max} = l_e/d_e = \sqrt{n_e/C_\infty}\sin(\theta/2)$. For PS, $C_\infty = 10$, and n_e = 327, which corresponds to M_e = 17 kg/mol. As a result, $\lambda_{max} = \sqrt{n_e/C_\infty}\sin(\theta/2) = 4.7$, and it is a good approximation of Λ = 4 in the experiments. In our simulations, λ_{max} = 4.8 with $C_\infty = 9.5$ (see Figure 2), and it is also a good approximation of Λ in the range 4.0−4.9.

The theoretical argument that Λ is determined by the maximum extension λ_{max} of an entanglement strand serves only as a good approximation. A detailed topological analysis of polymer chains during craze formation has shown that entanglements do not act as permanent chemical cross-links, but instead, their identities change by switching between different pairs of polymer chains and between different pairs of beads.[58] One hypothesis for $\Lambda_{CG} > \Lambda_{UA}$ is that the reduction in interchain friction weakens the effectiveness of topological constraints by enabling more identity changes of the constraints. This hypothesis needs further validation.

Following the determination of the craze extension ratio Λ, the stress−stretch curves in the CG and UA simulations are further compared by plotting σ_z/S against $(\lambda - 1)/(\Lambda - 1)$. As shown in Figure 7, the rescaled stress−stretch curves almost overlap with each other for $(\lambda - 1)/(\Lambda - 1) > 0.25$, indicating model-independent features of the stable craze growth until $(\lambda - 1)/(\Lambda - 1) = 1$ and the initial stretching of the craze fibrils for $(\lambda - 1)/(\Lambda - 1) > 1$. The rescaled curves at $(\lambda - 1)/(\Lambda - 1) < 0.25$ show that a higher σ_Y/S is required for the nucleation of craze fibrils in the UA simulation, and the crossover from the yield peak to the stress plateau takes place over a broader range of $(\lambda - 1)/(\Lambda - 1)$ in the UA simulation. These discrepancies reflect the effects of coarse-graining on yielding and craze nucleation.

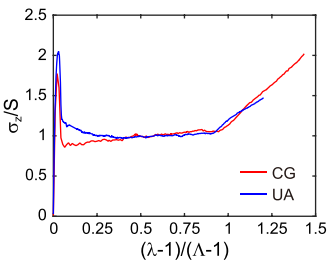

Figure 7. Normalized tensile stress σ_z/S as a function of $(\lambda - 1)/(\Lambda - 1)$ for the CG and UA samples. The extension ratios Λ_{CG} = 4.9 and Λ_{UA} = 4.2 are used in the normalization.

3.3. Craze Structure. The microstructure of craze is an important aspect of the microscopic description of crazing.[38,40−42] Craze fibrils at λ = 4.8 in the CG simulation and at λ = 5 in the UA simulation are used for the structural characterization. The two values of λ are close to each other, but are both larger than the respective values of Λ. Compared to the monomer density profile at $\lambda = \Lambda$, the monomer density profile at λ slightly larger than Λ has fewer fluctuations across the simulation box and is therefore more suitable for the structural characterization. As described in section 2.4, we characterize the craze structure in the simulations using two methods. In method I, monomers in one cross section of the simulation box are classified into clusters based on their separations. Each cluster represents the cross section of a craze fibril, as illustrated in Figures 8a and 8b for the CG and UA simulations, respectively. The corresponding probability density $P(D)$ of the fibril diameter D is shown in Figure 8c. The broad distribution of D indicates that the craze is not a forest of uniformly distributed fibrils of a constant diameter as described in the microscopic models of crazing.[38,40−42] $P(D)$ for the CG and UA samples closely track each other. The number-average fibril diameter $\langle D\rangle_{CG}$ = 35 Å for the CG sample and $\langle D\rangle_{UA}$ = 33 Å for the UA sample are almost the same. The area-average fibril diameter $\langle D\rangle^A_{CG}$ = 84 Å for the CG sample and $\langle D\rangle^A_{UA}$ = 81 Å for the UA sample are also almost the same. Experiments have also shown a broad distribution of PS craze fibril diameter. The range of D in the simulation covers the typical range of D from 40 to 100 Å in the experiments,[38] as indicated in Figure 8c.

In method II, the structure factor $S(k_\perp)$ is computed. As shown in Figure 9, $S(k_\perp)$ for the CG and UA samples are almost identical. Both follow the asymptotic Porod's scattering law $S(k_\perp) \sim k_\perp^{-3}$ in the range 0.05 Å$^{-1} \le k_\perp \le$ 0.5 Å^{-1}, as indicated by the dashed line in Figure 9. The data in the Porod's scaling regime can be used to compute an average fibril diameter, $\langle D\rangle = Q/\pi^3(1 - 1/\lambda)\alpha$,[48,94−96] where $Q = \int 2\pi k_\perp S(k_\perp)\, dk_\perp$ and α is the prefactor in the power law

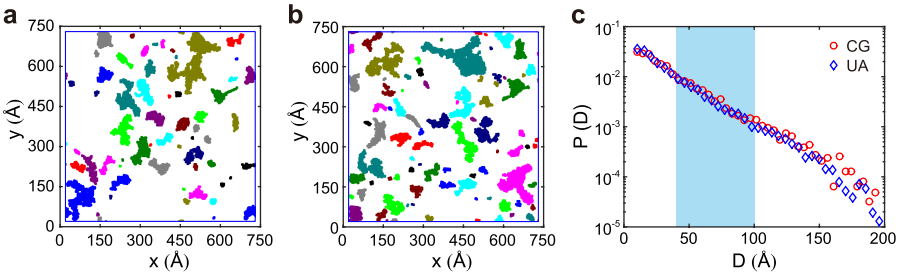

Figure 8. Cross section of a fully developed craze in (a) the CG simulation at λ = 5.0 and (b) the UA simulation at λ = 4.8. The blue squares in (a) and (b) indicate the simulation boxes with periodic boundary conditions. (c) Probability density $P(D)$ of the fibril diameter D for the craze in the CG and UA simulations. The typical range of D from 40 to 100 Å in experiments is indicated by the blue shaded region.

https://doi.org/10.1021/acs.macromol.1c01969
Macromolecules 2022, 55, 1267−1278

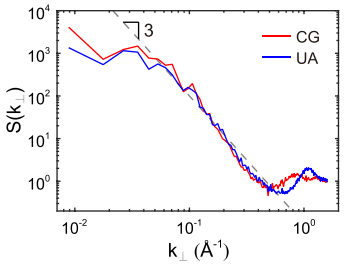

Figure 9. Structure factor $S(k_\perp)$ of the craze structure in the CG and UA simulations. The dashed line has a slope of −3.

$S(k_\perp) = \alpha k_\perp^{-3}$. The average fibril diameter from the Porod's analysis is 16.3 and 13.3 Å for the CG and UA samples in the simulations. The value of $\langle D \rangle$ based on small-angle X-ray scattering experiment of a PS craze is 60 Å.[38] Although the values of $\langle D \rangle$ in the simulations are smaller than the reported experimental value, $\langle D \rangle$ for the CG and UA samples are comparable to each other.

The average spacing between fibrils can be estimated in method I, as described in section 2.4. $\langle D_0 \rangle_{CG} = 102$ Å for the CG sample, and $\langle D_0 \rangle_{UA} = 90$ Å for the UA sample. The values for the two samples are close to each other and comparable to the average spacing d_e between the entanglements in PS. For $C_\infty = 10$, $n_e = 327$, and $l_0 = 1.574$ Å, $d_e = \sqrt{C_\infty n_e l_0^2} = 90$ Å. The result $\langle D_0 \rangle \approx d_e$ agrees with the theoretical argument[41,42] that the average spacing between fibrils is controlled by d_e. The argument results from the consideration that further increase of the spacing above d_e would break the entanglement network, which is energetically unfavorable. In experiment, the distance between the centers of nearest-neighboring craze fibrils were found to be in the range 200−300 Å based on TEM images, but measuring enough fibrils for good statistics is very tedious.[38] See Table 1 for the summary of simulation and experiment results of $\langle D \rangle$ and $\langle D_0 \rangle$.

3.4. Stress Decomposition and Surface Tension. The drawing stress can be decomposed into energetic and dissipative components, as shown in Figure 10. The energetic stress σ_z^U is defined as the derivative of internal energy density with respect to strain; i.e., $\sigma_z^U = \partial U/\partial \varepsilon_z$, where U is the internal energy per unit volume and $\varepsilon_z = (L_z - L_z^0)/L_z^0 = (\lambda - 1)$ is the engineering strain.[30] The dissipative stress σ_z^Q is the difference between the overall stress and the energetic stress; i.e., $\sigma_z^Q = \sigma_z - \sigma_z^U$. σ_z^U and σ_z^Q correspond to the increase of internal energy and the heat transfer. Coarse-graining lowers σ_z^U and σ_z^Q, which results from the decrease of the degrees of freedom that can store internal energy and the reduction of the energy barrier for plastic rearrangements, respectively. However, $\sigma_z^Q/\sigma_z \approx$ 81% and 74% during the craze growth in the CG and UA simulations, respectively. This suggests that although coarse-graining lowers both σ_z^U and σ_z^Q, it almost preserves the relative contributions from the internal energy change and energy dissipation to the stress during craze formation. The comparability of the relative contributions from σ_z^U and σ_z^Q is better shown by σ_z^U/S and σ_z^Q/S against $(\lambda - 1)/(\Lambda - 1)$ in Figure 10. Note that the craze growth is stable in both CG and UA simulations only for $0.25 < (\lambda - 1)/(\Lambda - 1) < 1$.

After the craze formation is completed (at $\lambda = \Lambda = 4.9$ and 4.2 for the CG and UA samples, respectively), σ_z^U remains almost unchanged until the end of the simulations, while σ_z^Q rises and results in the increase of the overall drawing stress σ_z. The rise of σ_z^Q for $\lambda > \Lambda$ reflects the increased rate of energy dissipation as the fully developed craze fibrils are further oriented toward the z-direction. The rise of σ_z^U would occur at λ beyond the simulation range, where the chain backbones would be stretched to increase the internal energy. The study of the stretching of PS chains to the breaking point requires force fields that allow bond breaking and is beyond the scope of this work.

Previous molecular models[38,40] of crazing describe the growth of craze as the propagation of voids into uncrazed dense glass and show that the drawing stress $S = c\Gamma/\langle D_0 \rangle$, where Γ is the surface tension of glassy polymer and c is a numerical prefactor. As in the molecular models, we evaluate the relations of S to Γ and $\langle D_0 \rangle$ in the simulations. We estimate Γ as $\Delta U_{nonbonded}/\Delta A$, where $\Delta U_{nonbonded}$ is the increase of the nonbonded potential energy during craze formation and ΔA is the new surface area created. $U_{nonbonded}$ equals the nonbonded pairwise interactions $U(r)$ between CG beads in the CG simulation, while it includes the pairwise Lennard-Jones potentials and the long-range Coulomb potential in the UA simulation. The method of computing ΔA is described in section 2.4. In the CG simulation, $\Delta U_{nonbonded} = 5.94 \times 10^6$ kJ/mol, $\Delta A = 4.6 \times 10^7$ Å^2, and $\Gamma_{CG} = 21.5$ mN/m. In the UA simulation, $\Delta U_{nonbonded} = 1.78 \times 10^7$ kJ/mol, $\Delta A = 5.4 \times 10^7$ Å^2, and $\Gamma_{UA} = 54.7$ mN/m. $\Gamma_{CG} < \Gamma_{UA}$ is another consequence of coarse-graining smoothing the potential energy landscape. As shown in Table 1, compared to the experimental value $\Gamma \approx 40$ mN/m,[97] Γ_{CG} is smaller while Γ_{UA} is larger. However, in both CG and UA simulations, the relation $S = c\Gamma/\langle D_0 \rangle$ in the molecular models of crazing is observed. Using $S_{CG} = 34$ MPa and $S_{UA} = 91$ MPa from section 3.1 and $\langle D_0 \rangle_{CG} = 102$ Å and $\langle D_0 \rangle_{UA} = 90$ Å from section 3.3, we obtain $S_{CG} = 16\Gamma_{CG}/\langle D_0 \rangle_{CG}$ and $S_{UA} = 15\Gamma_{UA}/\langle D_0 \rangle_{UA}$ with the values of c in the two simulations close to each other.

3.5. Scale-Bridging Simulations. While the stress level in the CG simulation is lower than that in the UA simulation, the

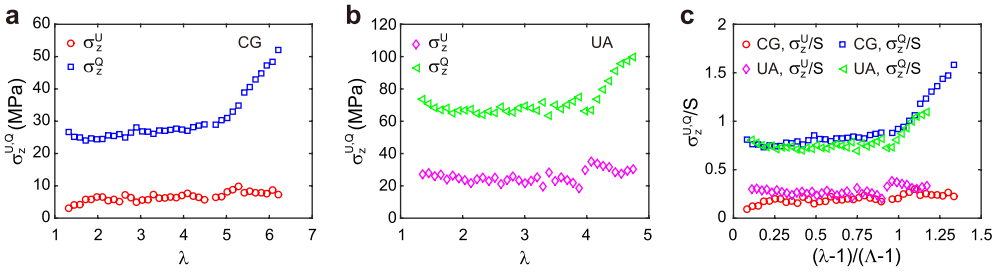

Figure 10. Tensile stress σ_z is decomposed into the energetic component σ_z^U and the dissipative component σ_z^Q for the (a) CG and (b) UA simulations. (c) σ_z^U and σ_z^Q normalized by S as functions of $(\lambda - 1)/(\Lambda - 1)$ for the CG and UA samples.

https://doi.org/10.1021/acs.macromol.1c01969
Macromolecules 2022, 55, 1267−1278

structural features of craze fibrils such as the extension ratio, fibril diameter, and spacing are almost the same in the two simulations. This allows us to develop a scale-bridging simulation protocol to accelerate the craze formation in the UA simulation. Similar to the scale-bridging protocol for the shear simulations of glassy PS,[30] the scale-bridging simulation of crazing consists of three steps. First, a CG simulation is performed to craze the PS glass up to an intermediate stretch factor, which is smaller than the craze extension ratio Λ. Subsequently, the CG sample with coexisting dense glass and craze fibrils is mapped to the UA representation by inserting the atomistic details that are removed in the CG model. An energy minimization follows the insertion, as in the equilibration of the UA sample back-mapped from the CG sample (see section 2.2). Finally, the crazing simulation is resumed with the UA representation. One example of the scale-bridging protocol is shown in Figure 11. The CG sample

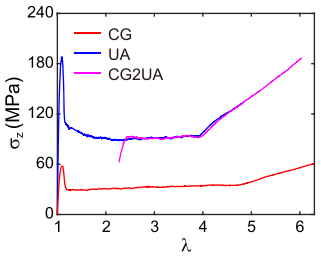

Figure 11. Demonstration of a scale-bridging simulation protocol. The CG sample was stretched to $\lambda = 2.2$ and then back-mapped to the UA representation. The resumed UA simulation recovers the stress level for the UA sample, as shown by the magenta stress−stretch curve.

at $\lambda = 2.2 < \Lambda = 4.9$ is back-mapped to the UA representation. The UA simulation restarted after an energy minimization brings the drawing stress to S_{UA} after an increase of 0.25 in λ. If the deformation on the UA sample was restarted after a long period, the sample would undergo aging dynamics to reach deeper local energy minima on the potential energy landscape. As a result, the yield stress after the UA simulation restarts would be increased to bring the system out of the deeper local energy minima. However, the postyield behavior would be identical with that of the current simulation without much aging, a phenomenon known as "rejuvenation". While aging and rejuvenation are interesting phenomena,[98] they are not essential to the effects of coarse-graining on the craze growth in the postyield regime and therefore are not studied here.

To quantify the computational efficiency of the CG and UA models, we compare the computing time of the CG and UA simulations. The computing time of the UA simulation from $\lambda = 1$ to $\lambda = 5$ with $\delta\lambda_{UA} = 4$ at loading velocity $v_{UA} = 2$ m/s was $t_{UA} = 2.9 \times 10^6$ CPU h. By contrast, the computing time of the CG simulation from $\lambda = 1$ to $\lambda = 6.6$ with $\delta\lambda_{CG} = 5.6$ at $v_{CG} = 1$ m/s was $t_{CG} = 0.6 \times 10^6$ CPU h. The computing times in the UA and CG simulations correspond to 280 and 58 days on 432 CPU cores, respectively. The long computing time reflects the state-of-the-art large scales of the well-entangled PS samples. For the same time step 0.002 ps, the total number of steps in the CG simulation is larger than that in the UA simulation by a factor of $(\delta\lambda_{CG}/v_{CG})/(\delta\lambda_{UA}/v_{UA}) = 2.8$. For the same number of steps, the CG model reduces the CPU time for the crazing simulation by a factor of $2.8 \times t_{UA}/t_{CG} \approx 13.5$. As the total number of atoms is reduced by a factor of 4 in the CG model, the rest of the speed-up factor $S^{UA-CG} \approx 13.5/4 \approx 3.4$ quantifies the acceleration due to the smoothing of the energy landscape by the coarse-graining. This result is consistent with the previous finding that $S^{UA-CG} \approx 3$ in the simulations of shearing PS glass.[30]

Because the CG model saves the computational resources by an order of magnitude, which results from the reduction of the total number of atoms by a factor of 4 and the speed-up factor $S^{UA-CG} \approx 3.4$ from the smoother energy landscape, the scale-bridging simulation protocol can significantly accelerate the simulations to obtain the craze structure and atomistic stress level at large λ. For shear deformation, our recent work[30] shows the stress−strain behavior of an all-atom (AA) sample at large shear strain can be recovered from the CG sample by using the scale-bridging simulation protocol. For crazing simulation, one would expect the craze structure and stress level for the AA sample may also be recovered from the CG sample by using the scale-bridging protocol.

4. CONCLUSIONS

We created and equilibrated state-of-the-art large-scale ($L_x = L_y = L_z \approx 71$ nm) CG and UA samples of well-entangled ($M_W \approx 10M_e$) PS melts. The samples were quenched to glassy states and crazed by using the conventional deformation protocols. A large amount of computing time was consumed to obtain the trajectories of PS crazing with atomistic details, especially the UA trajectory that corresponds to 280 days on 432 CPU cores. The results from the large-scale simulations of PS crazing are summarized and compared with the experimental data from the literature in Table 1. The values of the extension ratio Λ in the UA and CG simulations are both close to the experimental value. Λ is related to the maximum extension λ_{max} of a strand in the entanglement network as in the traditional models of craze formation. The values of the average fibril diameter $\langle D \rangle$ in the UA and CG simulations are almost the same and near the lower bound of the typical experimental values. The values of the average fibril spacing $\langle D_0 \rangle$ in the UA and CG simulations are both comparable to the average spacing between entanglements $d_e \approx 90$ nm, in consistence with the argument that $\langle D_0 \rangle$ is limited by d_e. The values of $\langle D_0 \rangle$ in the simulations are only half of the typical values in experiments.

The stress level in the CG simulation is reduced compared to that in the UA simulation, as the structure-based coarse-graining removes the degrees of freedom that can store energy and also lowers the energy barrier for plastic deformation. The use of a deformation rate much larger than the typical value in experiments brings the CG plateau stress S_{CG} close to the experimental value S_{exp}, but it makes the UA plateau stress S_{UA} about 3 times S_{exp}. The surface energy Γ_{CG} is smaller than the experimental value Γ_{exp}, while Γ_{UA} is larger than Γ_{exp}. However, in both CG and UA samples, the plateau stress and the surface energy are related to each other as $S = c\Gamma/\langle D_0 \rangle$ with $c = 15-16$, in agreement with the traditional theory for S. In addition, the dominance of the dissipative stress σ_z^Q over the energetic stress σ_z^U is preserved by the coarse-graining, reflecting comparable effects of the coarse-graining on reducing the degrees of freedom for energy storage and on lowering the barriers for energy dissipation.

For the coarse-grained PS model we use, the IBI method aims to keep the structural correlations between the styrene monomers in the atomistic simulations at thermal equilibrium. One would expect this feature of the IBI method is related to the structural similarities between the CG craze and the UA

https://doi.org/10.1021/acs.macromol.1c01969
Macromolecules 2022, 55, 1267−1278

craze in our simulations. However, more studies are needed to determine whether maintaining the structural correlations at thermal equilibrium is a necessary condition for the structural similarities during an out-of-equilibrium process. Other coarse-graining techniques, such as those based on force matching and relative entropy, have been used to develop CG models for the simulations on the equilibrium thermodynamic behavior of polymers. More studies are needed to determine the effects of different coarse-graining techniques on the mechanical behavior of polymers in out-of-equilibrium simulations.

In the CG model, a styrene monomer is mapped to two CG beads representing the backbone and side group, respectively. To increase the degree of coarse-graining, a styrene monomer may be mapped to one CG bead. However, the performance of the resulting CG model in the simulations of polymer mechanics has not been evaluated. It remains an intriguing question that what is the minimalist CG model for the simulations of polymer mechanics in large deformation and failure.

The use of the structure-based CG model facilitates the equilibration of the entanglement network. The subsequent back-mapping to the UA representation results in a well-entangled sample with atomistic details. For the generic coarse-grained bead−spring model, a similar hierarchical scheme has been used to equilibrate highly entangled polymer melts.[99,100] For chemically specific polymer models, a similar scheme based on the built-in coarse-grained model and all-atom replacement has been recently used to develop a builder that generates and equilibrates polymers for atomistic simulations.[101] In the context of fracture mechanics, CG simulation followed by the back-mapping to UA simulation also provides a faster route to obtain the microstructure of polymers with atomistic details and reach the atomistic stress level under deformation. In this scale-bridging approach, the CG component provides an interface with the bead−spring representation in polymer physics, whereas the atomistic component provides an interface with polymer chemistry. This scale-bridging approach may be potentially used to simulate the mechanical behavior of polymeric materials including polymer glass, elastomers, and gels and thus aid in the design of the material mechanics.

■ ASSOCIATED CONTENT

Supporting Information

The Supporting Information is available free of charge at https://pubs.acs.org/doi/10.1021/acs.macromol.1c01969

Movie captions (PDF)

Movie visualizing the craze formation in the CG simulation (MP4)

Movie visualizing the craze formation in the UA simulation (MP4)

■ AUTHOR INFORMATION

Corresponding Author

Ting Ge − *Department of Chemistry and Biochemistry, University of South Carolina, Columbia, South Carolina 29208, United States;* orcid.org/0000-0003-2456-732X; Email: tingg@mailbox.sc.edu

Authors

Jiuling Wang − *Department of Chemistry and Biochemistry, University of South Carolina, Columbia, South Carolina 29208, United States;* orcid.org/0000-0002-7379-3561

Pieter J. in 't Veld − *Soft Matter Modeling, BASF SE, 67056 Ludwigshafen, Germany;* orcid.org/0000-0001-8460-5688

Mark O. Robbins − *Department of Physics and Astronomy, Johns Hopkins University, Baltimore, Maryland 21218, United States*

Complete contact information is available at: https://pubs.acs.org/10.1021/acs.macromol.1c01969

Notes

The authors declare no competing financial interest.

■ ACKNOWLEDGMENTS

We thank Dominik Fritz for help with setting up the first coarse-grained simulation of polystyrene as well as Anupriya Agrawal and Gary S. Grest for sharing the tabulated forms of the coarse-grained force fields. T.G. acknowledges start-up funds from the University of South Carolina. This work was supported in part by the National Science Foundation EPSCoR Program under NSF Award OIA-1655740. Any opinions, findings and conclusions or recommendations expressed in this material are those of the authors and do not necessarily reflect those of the National Science Foundation. Simulations were performed on the Homewood High Performance Cluster at Johns Hopkins University, Maryland Advanced Research Computing Center, and the flagship computing cluster Hyperion at the University of South Carolina.

■ REFERENCES

(1) Peter, C.; Kremer, K. Multiscale simulation of soft matter systems—from the atomistic to the coarse-grained level and back. *Soft Matter* **2009**, *5*, 4357−4366.

(2) Li, Y.; Abberton, B. C.; Kröger, M.; Liu, W. K. Challenges in multiscale modeling of polymer dynamics. *Polymers* **2013**, *5*, 751.

(3) Rühle, V.; Junghans, C.; Lukyanov, A.; Kremer, K.; Andrienko, D. Versatile object-oriented toolkit for coarse-graining applications. *J. Chem. Theory Comput.* **2009**, *5*, 3211−3223.

(4) Reith, D.; Pütz, M.; Müller-Plathe, F. Deriving effective mesoscale potentials from atomistic simulations. *J. Comput. Chem.* **2003**, *24*, 1624−1636.

(5) Sun, Q.; Faller, R. Systematic coarse-graining of atomistic models for simulation of polymeric systems. *Comput. Chem. Eng.* **2005**, *29*, 2380−2385.

(6) Moore, T. C.; Iacovella, C. R.; McCabe, C. Derivation of coarse-grained potentials via multistate iterative Boltzmann inversion. *J. Chem. Phys.* **2014**, *140*, 224104.

(7) Lyubartsev, A. P.; Laaksonen, A. Calculation of effective interaction potentials from radial distribution functions: A reverse Monte Carlo approach. *Phys. Rev. E* **1995**, *52*, 3730−3737.

(8) Lyubartsev, A. P.; Karttunen, M.; Vattulainen, I.; Laaksonen, A. On coarse-graining by the inverse Monte Carlo method: Dissipative particle dynamics simulations made to a precise tool in soft matter modeling. *Soft Mater.* **2002**, *1*, 121−137.

(9) Ercolessi, F.; Adams, J. B. Interatomic potentials from first-principles calculations: the force-matching method. *Europhys. Lett.* **1994**, *26*, 583−588.

(10) Izvekov, S.; Parrinello, M.; Burnham, C. J.; Voth, G. A. Effective force fields for condensed phase systems from ab initio molecular dynamics simulation: A new method for force-matching. *J. Chem. Phys.* **2004**, *120*, 10896−10913.

(11) Izvekov, S.; Voth, G. A. Multiscale coarse graining of liquid-state systems. *J. Chem. Phys.* **2005**, *123*, 134105.
(12) Noid, W. G.; Chu, J.-W.; Ayton, G. S.; Voth, G. A. Multiscale coarse-graining and structural correlations: Connections to liquid-state theory. *J. Phys. Chem. B* **2007**, *111*, 4116−4127.
(13) Noid, W. G.; Chu, J.-W.; Ayton, G. S.; Krishna, V.; Izvekov, S.; Voth, G. A.; Das, A.; Andersen, H. C. The multiscale coarse-graining method. I. A rigorous bridge between atomistic and coarse-grained models. *J. Chem. Phys.* **2008**, *128*, 244114.
(14) Rudzinski, J. F.; Noid, W. G. Coarse-graining entropy, forces, and structures. *J. Chem. Phys.* **2011**, *135*, 214101.
(15) Shell, M. S. Coarse-graining with the relative entropy. *Adv. Chem. Phys.* **2016**, *161*, 395−441.
(16) Hsu, D. D.; Xia, W.; Arturo, S. G.; Keten, S. Thermomechanically consistent and temperature transferable coarse-graining of atactic polystyrene. *Macromolecules* **2015**, *48*, 3057−3068.
(17) Xia, W.; Song, J.; Jeong, C.; Hsu, D. D.; Phelan, F. R., Jr.; Douglas, J. F.; Keten, S. Energy-renormalization for achieving temperature transferable coarse-graining of polymer dynamics. *Macromolecules* **2017**, *50*, 8787−8796.
(18) Song, J.; Hsu, D. D.; Shull, K. R.; Phelan, F. R., Jr.; Douglas, J. F.; Xia, W.; Keten, S. Energy renormalization method for the coarse-graining of polymer viscoelasticity. *Macromolecules* **2018**, *51*, 3818−3827.
(19) Xia, W.; Hansoge, N. K.; Xu, W.-S.; Phelan, F. R.; Keten, S.; Douglas, J. F. Energy renormalization for coarse-graining polymers having different segmental structures. *Sci. Adv.* **2019**, *5*, No. eaav4683.
(20) Sherck, N.; Shen, K.; Nguyen, M.; Yoo, B.; Köhler, S.; Speros, J. C.; Delaney, K. T.; Shell, M. S.; Fredrickson, G. H. Molecularly informed field theories from bottom-up coarse-graining. *ACS Macro Lett.* **2021**, *10*, 576−583.
(21) Behbahani, A. F.; Schneider, L.; Rissanou, A.; Chazirakis, A.; Bačová, P.; Jana, P. K.; Li, W.; Doxastakis, M.; Polińska, P.; Burkhart, C.; Müller, M.; Harmandaris, V. A. Dynamics and Rheology of Polymer Melts via Hierarchical Atomistic, Coarse-Grained, and Slip-Spring Simulations. *Macromolecules* **2021**, *54*, 2740−2762.
(22) Harmandaris, V. A.; Kremer, K. Dynamics of polystyrene melts through hierachical multiscale simulations. *Macromolecules* **2009**, *42*, 791−802.
(23) Lyubimov, I. Y.; McCarty, J.; Clark, A.; Guenza, M. G. Analytical rescaling of polymer dynamics from mescoscale simulations. *J. Chem. Phys.* **2010**, *132*, 224903.
(24) Fritz, D.; Koschke, K.; Harmandaris, V. A.; van der Vegt, N. F. A.; Kremer, K. Multiscale modeling of soft matter: scaling of dynamics. *Phys. Chem. Chem. Phys.* **2011**, *13*, 10412−10420.
(25) Davtyan, A.; Dama, J. F.; Voth, G. A.; Andersen, H. C. Dynamic force matching: A method for constructing dynamical coarse-grained models with realistic time dependence. *J. Chem. Phys.* **2015**, *142*, 154104.
(26) Tschöp, W.; Kremer, K.; Batoulis, J.; Bürger, T.; Hahn, O. Simulation of polymer melts. I. Coarse-graining procedure for polycarbonates. *Acta Polym.* **1998**, *49*, 61−74.
(27) Tschöp, W.; Kremer, K.; Hahn, O.; Batoulis, J.; Bürger, T. Simulation of polymer melts. II. From coarse-grained models back to atomistic description. *Acta Polym.* **1998**, *49*, 75−79.
(28) Qian, H.; Carbone, P.; Chen, X.; Karimi-Varzaneh, H. A.; Liew, C. C.; Müller-Plathe, F. Temperature-transferable coarse-grained potentials for ethylbenzene, polystyrene, and their mixtures. *Macromolecules* **2008**, *41*, 9919−9929.
(29) Li, W.; Jana, P. K.; Behbahani, A. F.; Kritikos, G.; Schneider, L.; Polinska, P.; Burkhart, C.; Harmandaris, V. A.; Müller, M.; Doxastakis, M. Dynamics of long entangled polyisoprene melts via multiscale modeling. *Macromolecules* **2021**, *54*, 8693−8713.
(30) Ge, T.; Wang, J.; Robbins, M. O. Effects of coarse-graining on molecular simulations of mechanical properties of glassy polymers. *Macromolecules* **2021**, *54*, 2277−2287.
(31) Hansoge, N. K.; Gupta, A.; White, H.; Giuntoli, A.; Keten, S. Universal relation for effective interaction between polymer-grafted nanoparticles. *Macromolecules* **2021**, *54*, 3052−3064.
(32) Giuntoli, A.; Hansoge, N. K.; Keten, S. Star topology increases ballistic resistance in thin polymer films. *Extreme Mech. Lett.* **2020**, *41*, 101038.
(33) DeBenedictis, E. P.; Zhang, Y.; Keten, S. Structure and mechanics of bundled semiflexible polymer networks. *Macromolecules* **2020**, *53*, 6123−6134.
(34) Li, Z.; Xia, W. Coarse-grained modeling of nanocellulose network towards understanding the mechanical performance. *Extreme Mech. Lett.* **2020**, *40*, 100942.
(35) Alesadi, A.; Xia, W. Understanding the role of cohesive interaction in mechanical behavior of a glassy polymer. *Macromolecules* **2020**, *53*, 2754−2763.
(36) Xia, W.; Lan, T. Interfacial dynamics governs the mechanical properties of glassy polymer thin films. *Macromolecules* **2019**, *52*, 6547−6554.
(37) Rosch, T. W.; Brennan, J. K.; Izvekov, S.; Andzelm, J. W. Exploring the ability of a multiscale coarse-grained potential to describe the stress-strain response of glassy polystyrene. *Phys. Rev. E* **2013**, *87*, No. 042606.
(38) Kramer, E. J. Microscopic and molecular fundamentals of crazing. *Adv. Polym. Sci.* **1983**, *52*−*53*, 1−56.
(39) Brown, H. A molecular interpretation of the toughness of glassy polymers. *Macromolecules* **1991**, *24*, 2752−2756.
(40) Kramer, E. J.; Berger, L. L. Fundamental processes of craze growth and fracture. *Adv. Polym. Sci.* **1990**, *91/92*, 1−68.
(41) Krupenkin, T.; Fredrickson, G. Crazing in two and three dimensions. 1. Two-dimensional crazing. *Macromolecules* **1999**, *32*, 5029−5035.
(42) Krupenkin, T.; Fredrickson, G. Crazing in two and three dimensions. 2. Three-dimensional crazing. *Macromolecules* **1999**, *32*, 5036−5045.
(43) Estevez, R.; Tijssens, M.; Van der Giessen, E. Modeling of the competition between shear yielding and crazing in glassy polymers. *J. Mech. Phys. Solids* **2000**, *48*, 2585−2617.
(44) Creton, C.; Kramer, E. J.; Brown, H. R.; Hui, C.-Y. *Molecular Simulation Fracture Gel Theory*; Springer: 2001; pp 53−136.
(45) Socrate, S.; Boyce, M.; Lazzeri, A. A micromechanical model for multiple crazing in high impact polystyrene. *Mech. Mater.* **2001**, *33*, 155−175.
(46) Tiejun, W.; Kishimoto, K.; Notomi, M. Effect of triaxial stress constraint on the deformation and fracture of polymers. *Acta Mech. Sin.* **2002**, *18*, 480−493.
(47) Rottler, J.; Barsky, S.; Robbins, M. O. Cracks and crazes: on calculating the macroscopic fracture energy of glassy polymers from molecular simulations. *Phys. Rev. Lett.* **2002**, *89*, 148304.
(48) Rottler, J.; Robbins, M. O. Growth, microstructure, and failure of crazes in glassy polymers. *Phys. Rev. E* **2003**, *68*, No. 011801.
(49) Gearing, B.; Anand, L. On modeling the deformation and fracture response of glassy polymers due to shear-yielding and crazing. *Int. J. Solids Struct.* **2004**, *41*, 3125−3150.
(50) Rottler, J. Fracture in glassy polymers: a molecular modeling perspective. *J. Phys.-Condes. Matter* **2009**, *21*, 463101.
(51) Deblieck, R. A.; Van Beek, D.; Remerie, K.; Ward, I. M. Failure mechanisms in polyolefines: The role of crazing, shear yielding and the entanglement network. *Polymer* **2011**, *52*, 2979−2990.
(52) De Focatiis, D. S.; Buckley, C. P. Craze initiation in glassy polymers: Quantifying the influence of molecular orientation. *Polymer* **2011**, *52*, 4045−4053.
(53) Toepperwein, G. N.; de Pablo, J. J. Cavitation and crazing in rod-containing nanocomposites. *Macromolecules* **2011**, *44*, 5498−5509.
(54) Mahajan, D. K.; Hartmaier, A. Mechanisms of crazing in glassy polymers revealed by molecular dynamics simulations. *Phys. Rev. E* **2012**, *86*, No. 021802.
(55) Cheng, S.; Johnson, L.; Wang, S.-Q. Crazing and strain localization of polycarbonate glass in creep. *Polymer* **2013**, *54*, 3363−3369.

https://doi.org/10.1021/acs.macromol.1c01969
Macromolecules 2022, 55, 1267−1278

(56) Wang, S.-Q.; Cheng, S.; Lin, P.; Li, X. A phenomenological molecular model for yielding and brittle-ductile transition of polymer glasses. *J. Chem. Phys.* **2014**, *141*, No. 094905.
(57) Venkatesan, S.; Basu, S. Investigations into crazing in glassy amorphous polymers through molecular dynamics simulations. *J. Mech. Phys. Solids* **2015**, *77*, 123−145.
(58) Ge, T.; Tzoumanekas, C.; Anogiannakis, S. D.; Hoy, R. S.; Robbins, M. O. Entanglements in glassy polymer crazing: Cross-links or tubes? *Macromolecules* **2017**, *50*, 459−471.
(59) Jiang, H.; Zhang, J.; Yang, Z.; Jiang, C.; Kang, G. Modeling of competition between shear yielding and crazing in amorphous polymers' scratch. *Int. J. Solids Struct.* **2017**, *124*, 215−228.
(60) Razavi, M.; Cheng, S.; Huang, D.; Zhang, S.; Wang, S.-Q. Crazing and yielding in glassy polymers of high molecular weight. *Polymer* **2020**, *197*, 122445.
(61) Narayan, S.; Anand, L. Fracture of amorphous polymers: A gradient-damage theory. *J. Mech. Phys. Solids* **2021**, *146*, 104164.
(62) Haward, R. N.; Young, R. *The Physics of Glassy Polymers*, 2nd ed.; Springer: Netherlands, 1997.
(63) McCutcheon, C. J.; Zhao, B.; Jin, K.; Bates, F. S.; Ellison, C. J. Crazing mechanism and physical aging of poly(lactide) toughened with poly(ethylene oxide)-*block*-poly(butylene oxide) diblock copolymers. *Macromolecules* **2020**, *53*, 10163−10178.
(64) Baljon, A.; Robbins, M. O. Simulations of crazing in polymer glasses: Effect of chain length and surface tension. *Macromolecules* **2001**, *34*, 4200−4209.
(65) Rottler, J.; Robbins, M. O. Jamming under tension in polymer crazes. *Phys. Rev. Lett.* **2002**, *89*, 195501.
(66) Ge, T.; Grest, G. S.; Robbins, M. O. Tensile fracture of welded polymer interfaces: Miscibility, entanglements, and crazing. *Macromolecules* **2014**, *47*, 6982−6989.
(67) Ethier, J. G.; Drummy, L. F.; Vaia, R. A.; Hall, L. M. Uniaxial deformation and crazing in glassy polymer-grafted nanoparticle ultrathin films. *ACS Nano* **2019**, *13*, 12816−12829.
(68) Mondello, M.; Yang, H.-J.; Furuya, H.; Roe, R.-J. Molecular dynamics simulations of atactic polystyrene. 1. Comparison with X-ray scattering data. *Macromolecules* **1994**, *27*, 3566−3574.
(69) Agrawal, A.; Aryal, D.; Perahia, D.; Ge, T.; Grest, G. S. Coarse-graining atactic polystyrene and its analogues. *Macromolecules* **2014**, *47*, 3210−3218.
(70) Harmandaris, V. A.; Adhikari, N. P.; van der Vegt, N. F. A.; Kremer, K.; Mann, B. A.; Voelkel, R.; Weiss, H.; Liew, C. C. Ethylbenzene diffusion in polystyrene: United atom atomistic/coarse grained simulations and experiments. *Macromolecules* **2007**, *40*, 7026−7035.
(71) Fritz, D.; Harmandaris, V. A.; Kremer, K.; van der Vegt, N. F. A. Coarse-grained polymer melts based on isolated atomistic chains: Simulation of polystyrene of different tacticities. *Macromolecules* **2009**, *42*, 7579−7588.
(72) in't Veld, P. J. Enhanced Monte Carlo: A multi-purpose modular and easily extendable solution to molecular and mesoscale simulations. http://montecarlo.sourceforge.net.
(73) in 't Veld, P. J.; Rutledge, G. C. Temperature-dependent elasticity of a semicrystalline interphase composed of freely rotating chains. *Macromolecules* **2003**, *36*, 7358−7365.
(74) Harmandaris, V. A.; Adhikari, N. P.; van der Vegt, N. F. A.; Kremer, K. Hierarchical modeling of polystyrene: From atomistic to coarse-grained simulations. *Macromolecules* **2006**, *39*, 6708−6719.
(75) Santangelo, G.; Di Matteo, A.; Müller-Plathe, F.; Milano, G. From mesoscale back to atomistic models: A fast reverse-mapping procedure for vinyl polymer chains. *J. Phys. Chem. B* **2007**, *111*, 2765−2773.
(76) Spyriouni, T.; Tzoumanekas, C.; Theodorou, D.; Müller-Plathe, F.; Milano, G. Coarse-grained and reverse-mapped united-atom simulations of long-chain atactic polystyrene melts: Structure, thermodynamic properties, chain conformation, and entanglements. *Macromolecules* **2007**, *40*, 3876−3885.
(77) Ghanbari, A.; Bohm, M. C.; Muller-Plathe, F. A simple reverse mapping procedure for coarse-grained polymer models with rigid side groups. *Macromolecules* **2011**, *44*, 5520−5526.
(78) Wassenaar, T. A.; Pluhackova, K.; Böckmann, R. A.; Marrink, S. J.; Tieleman, D. P. Going backward: a flexible geometric approach to reverse transformation from coarse grained to atomistic models. *J. Chem. Theory Comput.* **2014**, *10*, 676−690.
(79) Krajniak, J.; Pandiyan, S.; Nies, E.; Samaey, G. Generic adaptive resolution method for reverse mapping of polymers from coarse-grained to atomistic descriptions. *J. Chem. Theory Comput.* **2016**, *12*, 5549−5562.
(80) Krajniak, J.; Zhang, Z.; Pandiyan, S.; Nies, E.; Samaey, G. Reverse mapping method for complex polymer systems. *J. Comput. Chem.* **2018**, *39*, 648−664.
(81) Zhang, G.; Chazirakis, A.; Harmandaris, V. A.; Stuehn, T.; Daoulas, K. C.; Kremer, K. Hierarchical modelling of polystyrene melts: from soft blobs to atomistic resolution. *Soft Matter* **2019**, *15*, 289−302.
(82) Li, W.; Burkhart, C.; Polińska, P.; Harmandaris, V.; Doxastakis, M. Backmapping coarse-grained macromolecules: An efficient and versatile machine learning approach. *J. Chem. Phys.* **2020**, *153*, No. 041101.
(83) Auhl, R.; Everaers, R.; Grest, G. S.; Kremer, K.; Plimpton, S. J. Equilibration of long chain polymer melts in computer simulations. *J. Chem. Phys.* **2003**, *119*, 12718−12728.
(84) Characteristic ratio of some polymers. https://polymerdatabase.com/polymer%20physics/C%20Table%20.html.
(85) Wang, J.; Ge, T. Crazing reveals an entanglement network in glassy ring polymers. *Macromolecules* **2021**, *54*, 7500−7511.
(86) Rottler, J.; Robbins, M. O. Yield conditions for deformation of amorphous polymer glasses. *Phys. Rev. E* **2001**, *64*, No. 051801.
(87) Thompson, A. P.; Aktulga, H. M.; Berger, R.; Bolintineanu, D. S.; Brown, W. M.; Crozier, P. S.; in 't Veld, P. J.; Kohlmeyer, A.; Moore, S. G.; Nguyen, T. D.; Shan, R.; Stevens, M. J.; Tranchida, J.; Trott, C.; Plimpton, S. J. LAMMPS - a flexible simulation tool for particle-based materials modeling at the atomic, meso, and continuum scales. *Comp Phys Comm* **2022**, *271*, 108171.
(88) Pastewka, L.; Robbins, M. O. Contact between rough surfaces and a criterion for macroscopic adhesion. *Proc. Natl. Acad. Sci. U. S. A.* **2014**, *111*, 3298−3303.
(89) Rottler, J.; Robbins, M. O. Shear yielding of amorphous glassy solids: Effect of temperature and strain rate. *Phys. Rev. E* **2003**, *68*, No. 011507.
(90) Rottler, J.; Robbins, M. O. Unified description of aging and rate effects in yield of glassy solids. *Phys. Rev. Lett.* **2005**, *95*, 225504.
(91) Vorselaars, B.; Lyulin, A. V.; Michels, M. Deforming glassy polystyrene: Influence of pressure, thermal history, and deformation mode on yielding and hardening. *J. Chem. Phys.* **2009**, *130*, No. 074905.
(92) Park, C.; Jung, J.; Yun, G. J. A multiscale micromorphic model with strain rate relationship between MD simulations and macroscale experimental tests and dynamic heterogeneity for glassy polymers. *Compos. Pt. B-Eng.* **2020**, *202*, 108439.
(93) Lyulin, A. V.; Balabaev, N. K.; Mazo, M. A.; Michels, M. Molecular dynamics simulation of uniaxial deformation of glassy amorphous atactic polystyrene. *Macromolecules* **2004**, *37*, 8785−8793.
(94) Brown, H. R.; Kramer, E. J. Craze microstructure from small-angle X-ray scattering (SAXS). *J. Macromol. Sci. Part B-Phys.* **1981**, *19*, 487−522.
(95) Paredes, E.; Fischer, E. W. Röntgenkleinwinkel-untersuchungen zur struktur der crazes (fließZonen) in polycarbonat und polymethylmethacrylat. *Makromol. Chem.* **1979**, *180*, 2707−2722.
(96) Brown, H. Polymer degradation by crazing and its study by small angle scattering techniques. *Mater. Sci. Rep.* **1987**, *2*, 317−370.
(97) Surface tensions of solid polymers. https://polymerdatabase.com/polymer%20physics/sigma.html.
(98) Roth, C. B. *Polymer Glasses*; CRC Press: 2016.

https://doi.org/10.1021/acs.macromol.1c01969
Macromolecules 2022, 55, 1267−1278

(99) Zhang, G.; Moreira, L. A.; Stuehn, T.; Daoulas, K. C.; Kremer, K. Equilibration of high molecular weight polymer melts: a hierarchical strategy. *ACS Macro Lett.* **2014**, *3*, 198−203.
(100) Hsu, H.-P.; Kremer, K. Efficient equilibration of confined and free-standing films of highly entangled polymer melts. *J. Chem. Phys.* **2020**, *153*, 144902.
(101) Choi, Y. K.; Park, S.-J.; Park, S.; Kim, S.; Kern, N. R.; Lee, J.; Im, W. CHARMM-GUI polymer builder for modeling and simulation of synthetic polymers. *J. Chem. Theory Comput.* **2021**, *17*, 2431−2443.

https://doi.org/10.1021/acs.macromol.1c01969
Macromolecules 2022, 55, 1267−1278